The structure of the magnetic reconnection exhaust boundary

Yi-Hsin Liu
Los Alamos National Laboratory, Los Alamos, NM 87545

J. F. Drake and M. Swisdak
University of Maryland, College Park, MD 20742

(Dated: February 19, 2022)

The structure of shocks that form at the exhaust boundaries during collisionless reconnection of anti-parallel fields is studied using particle-in-cell (PIC) simulations and modeling based on the anisotropic magnetohydrodynamic equations. Large-scale PIC simulations of reconnection and companion Riemann simulations of shock development demonstrate that the pressure anisotropy produced by counterstreaming ions within the exhaust prevents the development of classical Petschek switch-off-slow shocks (SSS). The shock structure that does develop is controlled by the firehose stability parameter $\varepsilon = 1 - \mu_0(P_\parallel - P_\perp)/B^2$ through its influence on the speed order of the intermediate and slow waves. Here $P_\parallel$ and $P_\perp$ are the pressure parallel and perpendicular to the local magnetic field. The exhaust boundary is made up of a series of two shocks and a rotational wave. The first shock takes ε from unity upstream to a plateau of 0.25 downstream. The condition $\varepsilon = 0.25$ is special because at this value the speeds of nonlinear slow and intermediate waves are degenerate. The second slow shock leaves $\varepsilon = 0.25$ unchanged but further reduces the amplitude of the reconnecting magnetic field. Finally, in the core of the exhaust ε drops further and the transition is completed by a rotation of the reconnecting field into the out-of-plane direction. The acceleration of the exhaust takes place across the two slow shocks but not during the final rotation. The result is that the outflow speed falls below that expected from the Walén condition based on the asymptotic magnetic field. A simple analytic expression is given for the critical value of ε within the exhaust below which SSSs no longer bound the reconnection outflow.

I. INTRODUCTION

Magnetic reconnection plays an important role in converting magnetic energy to plasma kinetic and thermal energy. The bulk of the energy released during reconnection takes place downstream of the magnetic X-line where reconnected field lines expand outwards to release their tension. Further, the geometry of the outflow exhaust ultimately determines the rate of reconnection, the narrow exhaust of the Sweet-Parker model producing slow reconnection and the open outflow exhaust proposed by Petschek producing fast reconnection [1]. Petschek specifically proposed that a pair of switch-off slow shocks (SSS) stand in the inflow into the exhaust and convert the released magnetic energy into the Alfvénic outflow and thermal energy. Magnetohydrodynamic simulations of reconnection with a localized resistivity imposed at the X-line confirmed the development of Petschek's open outflow configuration and the formation of SSSs at the exhaust boundaries [2]. Particle heating by these shocks has been proposed to cause the X-ray emission in solar flares [3, 4].

Magnetic reconnection also takes place in environments in which collisions are either weak or essentially absent. Observations of reconnection in the solar wind in particular seem to suggest that reconnection X-lines and associated exhausts grow to very large scales and resemble the open outflow geometry predicted by Petschek [5]. On the other hand, direct observations of SSSs in the Earth's magnetosphere and the solar wind are infrequent [6].

An important result of the simulations of collisionless reconnection and the resultant Hall reconnection model is the spontaneous formation of an open outflow configuration analogous to that predicted by Petschek. This configuration develops even without an *adhoc* localized resistivity [7, 8]. A key question is whether the fast rates of reconnection seen in the relatively small systems explored in simulations persist in very large systems. Scaling studies seem to suggest that collisionless reconnection remains fast in very large systems [9–11]. On the other hand, while Hall MHD simulations of collisionless reconnection reveal the formation of SSSs at the boundaries of reconnection exhausts, kinetic simulations (hybrid or PIC models) reveal that the reconnecting magnetic field never switches off as expected from the SSS model [12]. Since it is the release of magnetic energy downstream from the X-line that ultimately drives the outflow rather than the dynamics close to the X-line, the absence of the SSS in kinetic simulations calls into question the conjecture that fast collisionless reconnection actually can scale to very large systems. Thus, a key requirement for demonstrating that Hall reconnection can explain the fast release of energy that takes place in large systems is to pin down the specific mechanism driving the Alfvénic outflow.

It is well known from observations [13–15] and modeling [13, 16, 17] of anti-parallel magnetic reconnection that ions counterstream through the exhaust with relative velocities of the order of the Alfvén speed, increasing the plasma pressure parallel to the local magnetic field. The consequence of this increase in parallel pressure is the development

of a barrier in the pseudo-potential that describes the slow shock transition. This prevents the slow shock from switching-off the reconnecting magnetic field [18, 19]. For highly oblique slow shocks relevant to reconnection and where the upstream value of ε is unity the critical value of the firehose stability parameter ε_{cr} below which the SSS solution becomes inaccessible is given by

$$\varepsilon_{cr} = \frac{5\beta_u + 2}{5\beta_u + 5}, \tag{1}$$

where β_u is the ratio of the plasma to magnetic pressure upstream. If ε falls below this critical value anywhere within the exhaust, the SSS solution becomes inaccessible. ε does fall below this value in kinetic reconnection simulations [18]. The presence of the potential barrier to the formation of the SSS actually arises because of the formation of a new slow shock solution, which is characterized by intermediate Mach number $M_I = \sqrt{V_x^2 \mu_0 \rho / \varepsilon B_x^2} = 1$ both upstream and downstream [19]. We denote this as a 1,1 slow shock or 11-SS. This 11-SS can also switch off the magnetic field downstream but differs from the SSS where the downstream intermediate Mach number $M_{Id} < 1$. However, we show in the present manuscript that this shock solution cannot reduce ε below the critical value given in Eq. (1) and therefore can not explain the values of ε below ε_{cr} seen in the reconnection simulations [18].

Riemann simulations of the structure of slow shocks [18], in which a constant normal magnetic field is added to a Harris equilibrium [20, 21], have revealed that the value of ε downstream of the shock transition tends to form a plateau at a value of 0.25 and it was demonstrated that at this value the phase speeds of nonlinear intermediate and slow waves are degenerate [19]. It was suggested that the coupling to a rotational mode at $\varepsilon = 0.25$ produced turbulence at the ion inertial scale $d_i = c/\omega_{pi}$ that produced sufficient scattering of ions to prevent ε from falling below 0.25. However, neither the SSS nor the 11-SS can reduce ε from unity upstream to 0.25 downstream.

Here we present the results of a PIC reconnection simulation that is large enough to reveal the formation of an $\varepsilon = 0.25$ plateau. The structure of the shocks that make up reconnection exhausts are explored by comparing the results of these reconnection simulations with parallel Riemann simulations and analytic analysis based on the anisotropic MHD equations. We show that the exhaust boundary is defined by two slow shock transitions followed by an RD. An anomalous slow shock (A-SS) [22], in which $M_I \gtrsim 1$ both upstream and downstream, reduces the upstream tangential magnetic field and takes ε from unity upstream to 0.25. A second slow shock forms on the $\varepsilon = 0.25$ plateau and further reduces the tangential magnetic field. This degenerate slow shock (D-SS) is a special case of the 11-SS corresponding to $M_I = M_{SL} = 1$ both upstream and downstream, where M_{SL} is the slow mode Mach number. The D-SS forms a compound wave with a RD whose rotation onsets when ε begins to fall below 0.25. In the reconnection simulation the core of the exhaust becomes firehose unstable, which prevents further acceleration of the exhaust outflow by the RD. As a consequence, the exhaust velocity falls below the value expected based on the upstream Alfvén speed.

II. SIMULATION DETAILS AND RESULTS

The PIC simulation is performed with the $P3D$ code [23] with periodic boundary conditions. The initial state is a double-Harris configuration. However we focus on one current sheet of $B_z = -B_a \tanh(x/w_i)$ and $n = n_h \mathrm{sech}^2(x/w_i) + n_a$. The magnetic field is normalized to the asymptotic magnetic field B_a, the density to the Harris density n_h, velocities to the Alfvén speed $C_A \equiv B_a/\sqrt{\mu_0 m_i n_h}$, lengths to the ion inertial length $d_i \equiv \sqrt{m_i/\mu_0 n_h e^2}$, times to the inverse ion cyclotron frequency $\Omega_{ci}^{-1} \equiv m_i/B_a e$, and temperatures to $m_i C_A^2$. Other important parameters are $m_i/m_e = 25$, $c = 15$, $n_a = 0.2$, $w_i = 2$ and uniform initial $T_{i,e} = 0.25$, which imply that $\beta_a = 0.2$. The system size is $819.2 d_i \times 409.2 d_i$ resolved by grids 16384×8192 with 100 particles per cell. Particles are advanced with a time step $\Delta t = 0.01$.

In Fig. 1(a) is the out-of-plane current density J_y from a simulation with quasi-steady reconnection. The X-line is at the origin. The black contours are the in-plane magnetic field lines. The outflow exhaust forms a Petschek-like open-outflow configuration. In (b) we show the firehose stability parameter ε. The counterstreaming ions that have been widely documented in satellite observations of reconnection exhausts [13–15] drive the anisotropy toward the firehose threshold. The blue curves bound the region where $\varepsilon < 1$. The red color table marks the region where ε falls between 0.1 and 0.4. In the central region of the exhaust, marked by the green contour, is the firehose unstable region where $\varepsilon < 0.0$. The significant structure in the firehose unstable region suggests that this instability is active in the core of the exhaust [12, 24]. With increasing distance from the X-line the region where $0.1 < \varepsilon < 0.4$ widens. In (c) we show cuts of ε across the exhaust at four locations as marked in (b). The tendency to form a plateau at 0.25 is evident in spite of the turbulence from the firehose unstable region. Petschek's reconnection model requires the development of a standing SSS that propagates in the inflow frame at the phase speed of intermediate wave. Since the intermediate wave speed goes to zero when ε goes to zero, the formation of a slow shock at the exhaust boundary

is going to differ substantially from the traditional SSS. Similar plateaus at $\varepsilon = 0.25$ have been identified in Riemann simulations of slow shocks [18].

The structure of the exhaust and its boundaries are shown in greater detail in Fig. 2 where various physical quantities are plotted along the black cut in Fig. 1(b). The gradual drop in B_z (in (b)) beginning at the exhaust boundary and the corresponding rise in pressure (in (d)), with the total plasma and magnetic pressure (in (d)) being nearly constant, is clear evidence for the development of a slow shock at the exhaust boundary. However, the downstream B_z does not appear to be switched-off (*i.e.*, B_z does not drop to zero and remain zero in the core of the exhaust) as in a MHD SSS. The out-of-plane component B_y indicates the presence of the residual of the right-handed polarized dispersive whistler wave that coincides with the front of the SS transition. These whistler waves open the reconnection dissipation region into an Petschek-like configuration [25]. Near the center of the exhaust, B_y increases in a left-handed (LH) polarization sense, which is the expected signature of an intermediate mode. However a clear LH polarized intermediate mode has not developed. The outflow V_z (in (g)) is driven by the $\mathbf{J} \times \mathbf{B}$ force (magnetic tension) associated with the decrease in the magnetic field B_z and is linked to the jump in B_z by the Walén relation, $\mathbf{V}_{zd} - \mathbf{V}_{zu} = \pm\sqrt{\rho_u \varepsilon_u/\mu_0}(\mathbf{B}_{zd}/\rho - \mathbf{B}_{zu}/\rho_u)$, where the subscripts "u" and "d" indicate upstream and dowstream values of the parameters, respectively [26]. The Walén prediction matches the exhaust velocity very well (dot-dashed blue curve in (g)) in the regions where B_z decreases gradually outside of the core of the exhaust. However, contrary to the Walén prediction, no further increase in the outflow velocity occurs when $|B_z|$ decreases sharply to zero in the center of the exhaust. This is probably because the magnetic tension in this firehose unstable region is zero. The consequence is that the reconnection outflow speed is typically $\sim 40\%$ slower than the Alfvén speed based on the asymptotic magnetic field.

In order to get a better idea of how slow shocks and rotational waves propagate out from the central exhaust to a much larger distance ($\sim 100 d_i$) than can be achieved in a reconnection simulation, we compare the results of Fig. 2 with those from a quasi-1D Riemann problem in Fig. 3. The angle θ_{BN} between the upstream magnetic field and the shock normal for this simulation was taken to 75°, which is the approximate value just upstream of the exhaust boundary in Fig. 2(f). Data from this simulation was presented earlier [18]. The cuts are very similar to those obtained from the cuts across the reconnection exhaust but there are differences. In Fig. 3(a) the plateau in ε at 0.25 is much more developed and the region of firehose instability is much smaller than in the reconnection simulation. Unlike the results from reconnection, the downstream LH rotational wave in Fig. 3(b) has clearly developed. These rotational waves have been identified as the downstream dispersive wavetrains of slow shocks [27]. However, the wavelength of the oscillations has been shown to depend on the shock transition thickness, which is not consistent with the dispersive wavetrain hypothesis [18]. Finally in the Riemann solution the outflow continues to be linked to the variation in B_z, consistent with the Walén relation (see the dot-dashed blue curve in Fig. 3(g)). Again, this difference is likely because ε does not fall below the marginal firehose stability threshold in the Riemann simulation.

III. 1-D SHOCK SOLUTIONS

To understand the structure of the shocks that appear in the reconnection and Riemann simulations, we evaluate the possible transitions using the anisotropic Rankine-Hugoniot jump conditions. These follow from the moment integration of the Vlasov equation for a monatomic plasma assuming that the off-diagonal pressure components are negligible [19, 28, 29]:

$$[\rho V_x]_d^u = 0 \tag{2}$$

$$\left[\rho V_x^2 + P + \frac{1}{3}\left(\varepsilon + \frac{1}{2}\right)\frac{B^2}{\mu_0} - \varepsilon\frac{B_x^2}{\mu_0}\right]_d^u = 0 \tag{3}$$

$$\left[\rho V_x \mathbf{V}_t - \varepsilon\frac{B_x \mathbf{B}_t}{\mu_0}\right]_d^u = 0 \tag{4}$$

$$\left[\left(\frac{1}{2}\rho V^2 + \frac{5}{2}P + \frac{1}{3}(\varepsilon - 1)\frac{B^2}{\mu_0}\right)V_x - (\varepsilon - 1)\frac{B_x \mathbf{B}_t}{\mu_0}\cdot\mathbf{V}_t - (\varepsilon - 1)\frac{B_x^2}{\mu_0}V_x + Q_x\right]_d^u = 0 \tag{5}$$

$[...]_d^u$ indicates the difference between up- and downstream. The equations are written in the deHoffmann-Teller frame where the electric field vanishes, $\mathbf{E} = V_x \mathbf{B}_t - \mathbf{V}_t B_x = 0$. Quantities ρ, V_x, $\mathbf{V}_t$, B_x, $\mathbf{B}_t$ and Q_x are the mass density, velocity of the bulk flow in the normal direction ($\hat{x}$), velocity of the bulk flow in the tangential direction (y-z

plane), normal component of the magnetic field, tangential components of the magnetic field, and the heat flux in the x-direction. Here $P \equiv (P_{||} + 2P_{\perp})/3$. Even with a known upstream state, these jump relations still have free parameters ε_d and Q_{xd} for which we will use the measured values from the simulations. The observed Q_x does not jump across the SS transition of interest so we can discard it.

The anisotropic MHD equations can be further simplified in the case relevant for magnetic reconnection where the normal magnetic field B_x is much smaller than the upstream transverse field $\mathbf{B}_{tu}$. In this case the normal velocity V_x is of the order of $C_{Ax} = B_x/\sqrt{\mu_0\rho}$ and is therefore also small compared with the fast mode wave speed. The fast mode can then be eliminated from the equations and to lowest order. Eqs. (2)-(5) become

$$[\Gamma]_d^u = 0, \tag{6}$$

$$\left[P + \frac{1}{3}\left(\varepsilon + \frac{1}{2}\right)\frac{B_t^2}{\mu_0}\right]_d^u = 0, \tag{7}$$

$$\left[\Gamma^2\frac{\mathbf{B}_t}{\rho} - \varepsilon\frac{B_x^2\mathbf{B}_t}{\mu_0}\right]_d^u = 0, \tag{8}$$

$$\left[\frac{1}{2}\Gamma^2\frac{B_t^2}{\rho^2 B_x^2} + \frac{5}{2}\frac{P}{\rho} - \frac{2}{3}(\varepsilon - 1)\frac{B_t^2}{\mu_0\rho}\right]_d^u = 0, \tag{9}$$

where the constant mass flux has been written as $\Gamma = \rho V_x$ and $\mathbf{V}_t$ has been eliminated from the zero constraint on the electric field.

We first address why a SSS solution does not appear in either the reconnection or Riemann solutions. Since there is no reliable analytic model for the downstream value of ε, we use the values of ε from the simulations to explore the possible shock transitions. In Fig. 4(a), we plot ε versus B_z from the right half part of the 75° Riemann simulation and a similar simulation with $\theta_{BN} = 30°$ (black curves). In the 30° data B_z decreases steadily from its upstream value to zero. The SS transition in this simulation corresponds to a SSS in which $B_{zd} = 0$ [18]. In the 75° data B_z decreases down to around 0.67 where $\varepsilon = 0.25$ and then decreases further on the plateau where ε remains at 0.25. In this case, as we have discussed earlier, there is no SSS transition. To understand the reason for these differences, we study the SS solutions from Eqs. (6)-(9). For $\varepsilon_u = 1$ and $B_{zu} = 1$ we find the traditional SSS solution in which the upstream intermediate Mach number $M_{Iu} \equiv V_{xu}\sqrt{\mu_0\rho_u}/B_x$ is unity and the density compression across the shock $R_\rho \equiv \rho/\rho_u$, downstream transverse flow V_{zd}, and Mach number M_{Id} are given by

$$R_\rho = \frac{\beta_u}{2/5 + \beta_u}, \tag{10}$$

$$V_{zd} = \frac{B_{zu}}{\sqrt{\mu_0\rho_u}}, \tag{11}$$

$$M_{Id}^2 = \frac{1}{\varepsilon_d R_\rho}, \tag{12}$$

where β_u is the upstream value of $\beta = 2P_u/\mu_0 B_z^2$. Note that the solution is independent of the downstream value of ε. M_{Id} depends on ε_d only because the intermediate wave speed depends on this parameter.

The disappearance of the SSS solutions is due to the emergence of a new SS solution from Eqs. (6)-(9), an $M_{Iu} = M_{Id} = 1$ transition that prevents the SSS solution from reaching $B_{zd} = 0$ [19]. Eqs. (6)-(9) yield the jump conditions on the density and magnetic field,

$$R_\rho = \frac{1}{\varepsilon_d}, \tag{13}$$

$$R_B = \frac{B_{zd}}{B_{zu}} = \frac{\frac{5}{2}\varepsilon_d - 1 - \frac{5}{2}(1 - \varepsilon_d)\beta_u}{\frac{1}{3}\varepsilon_d(1 + \frac{7}{2}\varepsilon_d)}. \tag{14}$$

This 11-SS solution is shown in the red lines in Fig. 4(a) as obtained from Eqs. (2)-(5). Note that the 11-SS does not intersect the measured $B_z - \varepsilon$ curve for the 30° case at a point other than the upstream state, but does for 75°. If the 11-SS solution intersects the $B_z - \varepsilon$ curve the SSS solution is no longer accessible. This is because the presence of the 11-SS solution at a finite value of B_{zd} signifies the formation of a minimum in the effective potential $\psi(B_y, B_z)$ that describes the SSS transition and a corresponding maximum at the origin where $B_z = B_y = 0$ [19]. The potential in this case is similar to that shown in Fig. 5(b). The survival of the SSS solution therefore requires that the minimum of ε_d as determined from either simulation or observational data fall above the minimum of ε that is accessible by the 11-SS. This minimum is obtained from Eq. (14) by taking $B_{zd} = 0$. Thus, the SSS can form as long as the minimum of ε across the outflow exhaust exceeds

$$\varepsilon_{cr} = \frac{5\beta_u + 2}{5\beta_u + 5}. \tag{15}$$

Thus, in the case of anti-parallel reconnection where counterstreaming ions reduce ε below this critical value there is no SSS transition. On the other hand, it is also evident from Fig. 4(a) that the 11-SS can not produce a transition below the minimum value given in Eq. (15), which lies above the 0.25 measured in the simulations.

The only option remaining for finding a SS solution that can transition to $\varepsilon_d = 0.25$ is to increase the value of the upstream Mach number M_{Iu} above unity. That increasing M_{Iu} facilitates a SS transition to a lower value of ε_d and is shown in Fig. 4(b), which shows the $B_z - \varepsilon$ relation obtained from Eqs. (2)-(5) for $M_{Iu} = 1.29$. The value of M_{Iu} was increased until the shock transition curve intersected the black curve at the red circle ($B_{z,d} = 0.67, \varepsilon_d = 0.25$). This super-intermediate SS transition, which was earlier denoted as an anomalous slow shock (A-SS) [22] is a possible solution for the SS seen in the 75° Riemann simulation. A similar solution with $M_{Iu} = 1.17$ that results in an intersection point ($B_{z,d} = 0.65, \varepsilon_d = 0.25$) is shown with the data from the reconnection simulation in Fig. 4(c).

To further test the hypothesis that the A-SS describes the reconnection exhaust boundary, we plot the downstream predictions of the A-SS transition based on Eqs. (2)-(5) on top of the data from the Riemann and reconnection simulations in Fig. 2 and 3. The predicted jumps of the A-SSs appear as dotted black lines, and they should be compared with the solid black lines. Overall, the predicted jumps of these A-SS's agree very well with the observed transitions. With the measured inflow speeds V_{ix}, which are ~ 0.3 and ~ 0.11 in Figs. 2(g) and 3(g), respectively, we can calculate the shock speeds of these A-SS's in the rest frame of the far upstream plasma. The local intermediate Mach number M_I is then derived and plotted in (h). The choice of M_{Iu} being slightly greater than unity and the shock therefore being super-intermediate is consistent with both the reconnection and Riemann simulations but is most evident in the Riemann case. The measured downstream Mach number in Fig. 2 (h), although oscillating, is comparable to the prediction, while it agrees very well in Fig. 3 (h). Our interpretation of why the shock is super-intermediate is that the ions stream along the local magnetic field and into the upstream at the Alfvén speed while encountering a weak inflowing plasma. The interaction between these two oppositely moving constituents would naturally drive the formation of a weak super-intermediate slow shock rather than the conventional standing slow shock.

A better understanding of the A-SS transition can be obtained from the pseudo-potential that describes the shock transition. This potential describes the variation of $\mathbf{B}_t$ as a function of the space variable in the 2-D $B_y - B_z$ plane. In analogy with 2-D particle dynamics, the space variable can be treated as time and the $B_y - B_z$ plane can be treated as a 2-D configuration space. We calculate the potential using the anisotropic derivative nonlinear-Schrödinger-Burgers equation [19]. To do this we need an analytic relation between B_z and ε. For simplicity we use a straight line from the upstream-to downstream states shown in Fig. 3(b) (Fig. 5(a)). The resulting pseudo-potential is shown in Fig. 5(b). In this potential a pseudo-particle starts at an upstream state B_{zu} and slides down the hill to B_{zd} with $B_y = 0$. The peak in the potential around $B_z = 0$ is evident. This potential hill prevents the A-SS from making a transition to $B_z = 0$. The pseudo-particle could, in principle, follow the valley by rotating B_z into B_y. However, as discussed below, this rotation does not take place at this location but further downstream.

The A-SS shock speed (solid red) and the variation of the intermediate λ_I (dot-dashed blue) and slow λ_{SL} (dot-dashed red) wave speeds across the transition are shown in Fig. 5(c). All velocities are shown in the upstream intermediate frame. Note that upstream the A-SS is super-intermediate and super-slow (the shock speed at B_{zu} exceeds the intermediate and slow characteristic speeds) and that downstream the A-SS is super-intermediate and sub-slow (the shock speed at B_{zd} exceeds the intermediate but is below the slow-characteristic speed). Thus, this A-SS is an $M_{Iu} > 1$ to $M_{Id} > 1$ transition with $M_{Id} > M_{Iu}$ as is evident in panel (h) of Figs. 2 and 3.

Two other distinct features of the exhaust boundaries are also evident in Figs. 2 and 3. In the $\varepsilon = 0.25$ pedestal region the transverse magnetic field B_z continues to decrease and the exhaust velocity continues to increase, the latter being consistent with the Walén prediction. Finally, further towards the symmetry line the transverse magnetic field B_z abruptly begins to rotate into the y-direction. The pedestal region with constant $\varepsilon = 0.25$ can again be explored with Eqs. (6)-(9). This case is a special case of the 11-SS solution discussed earlier. As in that solution,

$M_I = \sqrt{\Gamma^2\mu_0/\varepsilon\rho B_x^2}$ is a constant so that $\rho \propto \varepsilon^{-1}$ is constant. The energy equation then takes the form

$$\varepsilon(\varepsilon - \frac{1}{4})\left[\frac{B_z^2}{\mu_0}\right]_d^u = 0. \tag{16}$$

This equation reveals the unusual conditions that arise when $\varepsilon = 0.25$. This SS solution can support arbitrary changes in the transverse magnetic field and associated pressure (determined by the constancy of the magnetic plus plasma pressure). The existence of this transition is marked by the short horizontal red segment at 0.25 in Fig. 4(b). The transition is less evident in Fig. 4(c) because of the limited spatial extension in the normal direction of the reconnection simulation. Since ρ is a constant the transverse flow is given by the simplified Walén relation $[V_z]_d^u = \sqrt{\varepsilon/\mu_0\rho}[B_z]_d^u$. The condition of constant $\varepsilon = 0.25$ corresponds to the degeneracy of slow and intermediate waves [19]. We therefore refer to this solution as a degenerate slow shock (D-SS). Note that an exactly horizontal transition at $B_z - \varepsilon$ plane (*i.e.,* caused by scattering [18, 19]) can only take place at $\varepsilon = 0.25$ in the form of the D-SS. The pseudo-potential can again be constructed for the D-SS. The chosen $B_z - \varepsilon$ relation is shown by the dashed red curve in Fig. 5(d). It is a horizontal line from B_{zu} to B_{zd} and then is taken to $\varepsilon = 0$ at $B_z = 0$. The latter segment is meant to be illustrative. The structure of the pseudo-potential and characteristic speeds shown in Figs. 5(e-f) are insensitive to the detailed variation of ε as long as it drops below 0.25. Fig. 5(e) reveals that the potential is flat on the $\varepsilon = 0.25$ plateau and again has a barrier around the origin that prevents a direction transition to $B_z = 0$. On the plateau the shock, intermediate and slow wave speeds are equal to the upstream intermediate speed (Fig. 5(f)). The predicted weak jumps of D-SS (dotted red) of the Riemann simulation in Fig. 3 are added to jumps of A-SS (dotted black) for further comparison with data. The agreement between the simulation data and the D-SS predictions are reasonably good.

The data from both the reconnection and Riemann simulations reveal the remnant upstream tangential magnetic B_z abruptly begins a LH rotation at the lower edge of the ε plateau. This is especially evident in the Riemann simulations. The transition of the coplanar D-SS to this LH rotational mode follows from the structure of the pseudo-potential in Fig. 5(e). The pseudo-particle moves toward lower B_z but must rotate as a result of the barrier around the origin. Fig. 5(f) reveals that, as expected, the downstream intermediate characteristic speed decreases with decreasing ε and it becomes slower than the slow characteristic speed. The rotational mode is not an intermediate shock (IS) which must be super-intermediate upstream and sub-intermediate downstream (*i.e.,* the blue portion in Fig. 5(c)). Thus, the rotational wave should be interpreted as a rotational discontinuity (RD) that is linked to the D-SS, forming a compound D-SS/RD. The rate of rotation in the Riemann simulation is significantly higher than that in the reconnection simulation. This is likely because ε falls to zero in the core of the exhaust in the reconnection simulation, which reduces the rotation rate of the LH wave.

The dynamical picture leading to these multiple structures can be understood as following: The counter-streaming ions drives the overall tendency to form a A-SS + RD wave (Fig. 5(c)). However, due to rotation-induced scattering the ε tends to form a plateau at 0.25 [18, 19] and the downstream region locally evolves into a D-SS/RD compound wave (Fig. 5(f)).

IV. IMPLICATION

For a density of $1.0cm^{-3}$, typical of the magnetotail, $1d_i = 150km$, which implies that the simulation shown in Fig. 1 corresponds to roughly $20R_E$. During times when the tail has a single large X-line, the signatures discussed in this paper should be observable by Geotail and THEMIS. Specifically, we predict that no switch-off-slow shocks should develop if the measured values of ε across the exhaust fall below the threshold ε_{cr} given in Eq. (1). We predict that the exhaust boundary will exhibit two distinct SS transitions. The first is an anomalous slow shock (A-SS) that is a super-intermediate to super-intermediate transition that drops ε from unity to around 0.25. The second is a degenerate slow-shock (D-SS)/rotational-discontinuity (RD) compound wave that forms on and maintains a plateau with $\varepsilon = 0.25$. When $\varepsilon = 0.25$ the slow and intermediate wave speeds are equal and the resulting D-SS can support an isobaric change in magnetic and particle pressure while leaving the density constant. The RD rotates the residual transverse magnetic field in the left-hand sense. Since the cross-exhaust width of the firehose unstable region does not increase with distance downstream of the X-line in reconnection simulation, we suggest that the dissipation region proper is the source of the firehose unstable region. This firehose unstable region causes the failure of Walén relation.

Several caveats must be kept in mind. First, because of the relatively narrow angle of the reconnection outflow exhaust, small reconnection events might be too narrow for the $\varepsilon = 0.25$ plateau to develop. Second, we have only considered 2D simulations that are invariant in the y direction. A more realistic 3D system may develop other features that mask or even change our conclusions. Finally, unlike the anti-parallel case, with a significant ambient initial guide field B_y the firehose parameter ε does not become as small and as will be shown in a future manuscript a pair of RD's switch off the reconnecting magnetic field (B_z).

Acknowledgments

Y. -H. L. acknowledges helpful discussions with W. Daughton, H. Karimabadi and L. Hui. This work was supported in part by NASA grant Nos. NNX08AV87G, NNX09A102G, NASA's Heliophysics Theory Program and a grant from the DOE/NSF partnership in basic plasma physics. Computations were carried out at the National Energy Research Scientific Computing Center. LA-UR-11-12116.

Appendix: Exact solutions of the anisotropic MHD equations

Equations (2)-(5) have analytic solutions,

$$A_x^2 \equiv \frac{V_x^2}{B_x^2/(\mu_0\rho)} = \frac{-b \pm \sqrt{b^2-4ac}}{2a}, \tag{17}$$

where

$$a = \frac{2}{5}\frac{B^2}{B_x^2}, \tag{18}$$

$$b = -A_{xu}^2 - \left[\frac{\beta_u}{2} + \frac{1}{3}(\varepsilon_u + \frac{1}{2})\right]\sec^2\theta_u + \varepsilon_u - \left[\frac{3}{5}\frac{B_t}{B_x} - \frac{2}{5}\frac{B_x}{B_t}\right]\tan\theta_u(A_{xu}^2 - \varepsilon_u) - \frac{1}{10}\frac{B^2}{B_x^2}, \tag{19}$$

$$c = \frac{1}{5}\sec^2\theta_u A_{xu}^4 + \left[\frac{\beta_u}{2} - \frac{4}{15}(\varepsilon_u - 1)\right]\sec^2\theta_u A_{xu}^2, \tag{20}$$

where Q_x has been neglected. Using the identity

$$\varepsilon = A_x^2 - \tan\theta_u \frac{B_x}{B_t}(A_{xu}^2 - \varepsilon_u) \tag{21}$$

with given θ_u, β_u, ε_u and A_{xu}, we can plot ε versus B_t and obtain the following jump conditions.

$$M_I = \frac{A_x}{\sqrt{\varepsilon}}, \tag{22}$$

$$\frac{\rho}{\rho_u} = \frac{A_{xu}^2}{A_x^2}, \tag{23}$$

$$\frac{\beta}{\beta_u} = \frac{2B_x^2}{\beta_u B^2}\left\{A_{xu}^2 + \left[\frac{\beta_u}{2} + \frac{1}{3}(\varepsilon_u + \frac{1}{2})\right]\sec^2\theta_u - \varepsilon_u - A_x^2 + \varepsilon\right\} - \frac{2}{3\beta_u}(\varepsilon + \frac{1}{2}), \tag{24}$$

$$\frac{P}{P_u} = \left(\frac{\beta}{\beta_u}\right)\frac{B^2}{B_x^2}\cos^2\theta_u, \tag{25}$$

and the downstream transverse velocity measured at upstream plasma frame,

$$\frac{V_t}{B_x/\sqrt{\mu_0\rho_u}} = A_{xu}\tan\theta_u - \frac{B_t}{B_x}\frac{A_x^2}{A_{xu}}. \tag{26}$$

In the very oblique limit, we look for solution of $A_{xu}^2 = \varepsilon_u$ and $A_x^2 = \varepsilon$ (the 11-SS solution). $B_t = 0$ is further imposed, since this point gives us the minimum ε_{cr} of 11-SS transitions. We get

$$a \sim \frac{2}{5}, \tag{27}$$

$$b \sim -\left[\frac{\beta_u}{2} + \frac{1}{3}(\varepsilon_u + \frac{1}{2})\right] \sec^2\theta_u, \tag{28}$$

$$c \sim \left\{\frac{1}{5}\varepsilon_u^2 + \left[\frac{\beta_u}{2} - \frac{4}{15}(\varepsilon_u - 1)\right]\varepsilon_u\right\} \sec^2\theta_u. \tag{29}$$

Plug these into Eq. (17), choose the plus sign and expand it, the minimum ε_{cr} value that a SSS (with a given ε_u and β_u) can transition to is obtained

$$\varepsilon_{cr} = A_x^2 \sim \frac{c}{|b|} = \frac{-2\varepsilon_u^2 + (15\beta_u + 8)\varepsilon_u}{10\varepsilon_u + 15\beta_u + 5}. \tag{30}$$

Eq. (1) is re-derived when $\varepsilon_u = 1$,

$$\varepsilon_{cr} = \frac{5\beta_u + 2}{5\beta_u + 5}. \tag{31}$$

We noticed that $\varepsilon_u - \varepsilon_{cr} > 0$ vanishes when ε_u approaches value 0.25 from unity. Therefore $\varepsilon = 0.25$ is the solution of $\varepsilon_u = \varepsilon_{cr}$. From this we can conclude that a SSS with a $\varepsilon_u > 0.25$ and an arbitrary β_u can not transition to $\varepsilon < 0.25$ region. In other words, 0.25 is an "absolute" barrier across which a SSS with $\varepsilon_u > 0.25$ can not cross.

[1] H. E. Petschek, in *Proc. AAS-NASA Symp. Phys. Solar Flares* (1964), vol. 50 of *NASA-SP*, pp. 425–439.
[2] T. Sato and T. Hayashi, Phys. Fluids **22**, 1189 (1979).
[3] S. Tsuneta, Astrophys. J. **456**, 840 (1996).
[4] D. W. Longcope and S. E. Guidoni, Astrophys. J. **740**, 73 (2011).
[5] T. D. Phan, J. T. Gosling, M. S. Davis, R. M. Skoug, M. Øieroset, R. P. Lin, R. P. Lepping, D. J. McComas, C. W. Smith, H. Rème, et al., Nature **439**, 175 (2006).
[6] J. Seon, L. A. Frank, W. R. Paterson, J. D. Scudder, F. V. Coroniti, S. Kokubun, and T. Yamamoto, J. Geophys. Res. **101**, 27383 (1996).
[7] R. G. Kleva, J. F. Drake, and F. L. Waelbroeck, Phys. Plasmas **2**, 23 (1995).
[8] Z. W. Ma and A. Bhattacharjee, Geophys. Res. Lett. **23**, 1673 (1996).
[9] M. A. Shay, J. F. Drake, B. N. Rogers, and R. E. Denton, Geophys. Res. Lett. **26**, 2163 (1999).
[10] M. A. Shay, J. F. Drake, M. Swisdak, and B. N. Rogers, Phys. Plasmas **11**, 2199 (2004).
[11] M. A. Shay, J. F. Drake, and M. Swisdak, Phys. Rev. Lett. **99**, 155002 (2007).
[12] R. F. Lottermoser, M. Scholer, and A. P. Matthews, J. Geophys. Res. **103**, 4547 (1998).
[13] M. Hoshino, T. Mukai, and T. Yamamoto, J. Geophys. Res. **103**, 4509 (1998).
[14] J. T. Gosling, R. M. Skoug, D. J. McComas, and C. W. Smith, J. Geophys. Res. **110**, A01107 (2005).
[15] T. D. Phan, G. Paschmann, C. Twitty, F. S. Mozer, J. T. Gosling, J. P. Eastwood, M. Øieroset, H. Rème, and E. A. Lucek, Geophys. Res. Lett. L14104 (2007).
[16] K. Arzner and M. Scholer, J. Geophys. Res. **106**, 3827 (2001).
[17] J. F. Drake, M. Swisdak, T. D. Phan, P. A. Cassak, M. A. Shay, S. T. Lepri, R. P. Lin, E. Quataert, and T. H. Zurbuchen, J. Geophys. Res. **114**, 05111 (2009).
[18] Yi-Hsin Liu, J. F. Drake, and M. Swisdak, Phys. Plasmas **18**, 062110 (2011).
[19] Yi-Hsin Liu, J. F. Drake, and M. Swisdak, submitted to POP (2011).
[20] Y. Lin and L. C. Lee, Space Science Reviews **65**, 59 (1993).
[21] M. Scholer and R. F. Lottermoser, Geophys. Res. Lett. **25**, 3281 (1998).
[22] H. Karimabadi, D. Krauss-Varban, and N. Omidi, Geophys. Res. Lett. **22**, 2689 (1995).
[23] A. Zeiler, D. Biskamp, J. F. Drake, B. N. Rogers, M. A. Shay, and M. Scholer, J. Geophys. Res. **107**, 1230 (2002).
[24] H. Karimabadi, D. Krauss-Varban, N. Omidi, and H. X. Vu, J. Geophys. Res. **104**, 12313 (1999).
[25] J. F. Drake, M. A. Shay, and M. Swisdak, Phys. Plasmas **15**, 042306 (2008).
[26] B. U. O. Sonnerup, G. Paschmann, I. Papamastorakis, N. Sckopke, G. Haerendel, S. Bame, J. R. Asbridge, J. T. Gosling, , and C. T. Russell, J. Geophys. Res. **86**, 10049 (1981).
[27] F. V. Coroniti, Nucl. Fusion **11**, 261 (1971).
[28] J. K. Chao, Rep. CSR TR-70-s, Mass. Inst. of Technology. Cent. for Space Res., Cambridge, Mass. (1970).
[29] P. D. Hudson, Planetary and Space Science **18**, 1611 (1970).

Figures

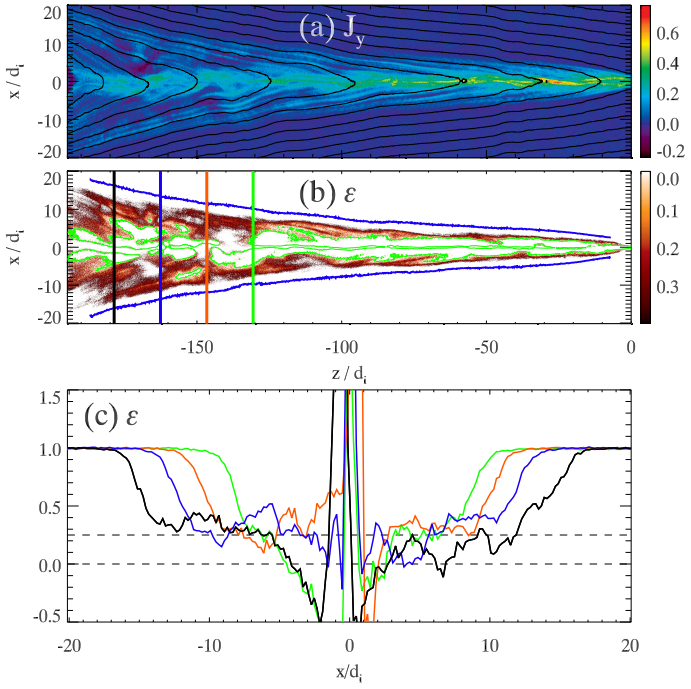

FIG. 1: In (a) the out-of-plane current density J_y overlaid with the in-plane magnetic field. In (b) the pair of blue curves bound the region $\varepsilon < 1$, the red colored areas have $0.1 < \varepsilon < 0.4$ and the green curves bound regions with $\varepsilon < 0.0$. In (c) are cuts of ε at four locations marked in (b). Note the tendency to form a plateau at 0.25.

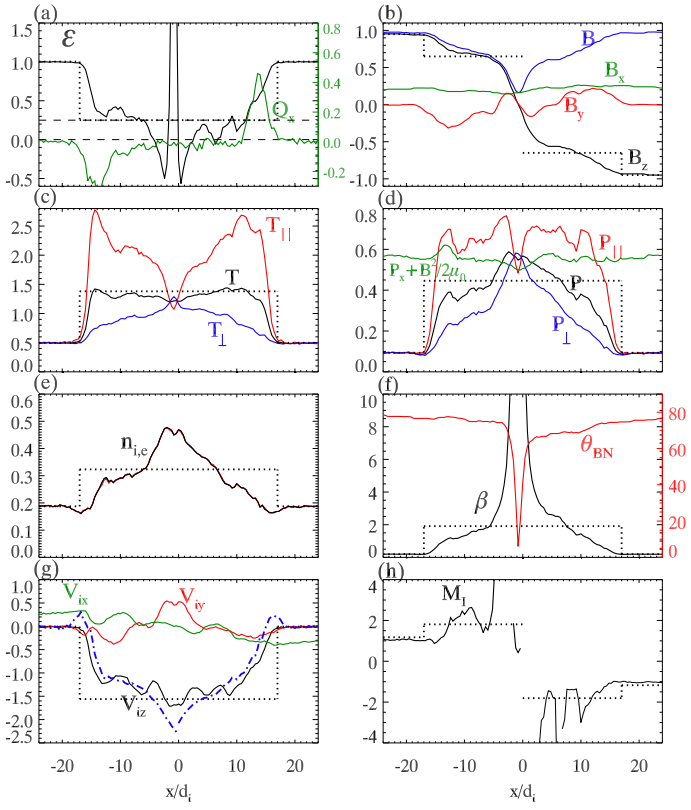

FIG. 2: From the reconnection simulation profiles of physical quantities along the black cut of Fig. 1(b). ε and Q_x in (a), B's in (b), T's in (c), P's in (d), n_i and n_e in (e), β and θ_{BN} in (f), V's in (g) and M_I in (h). θ_{BN} is the angle between the local magnetic field and the x-direction. The dot-dashed blue curve in (g) is the Walén relation. The dotted black curves are the predicted jumps of an anomalous slow shock with $M_{Iu} = 1.17$, and these dotted curves should be compared with the solid black curves.

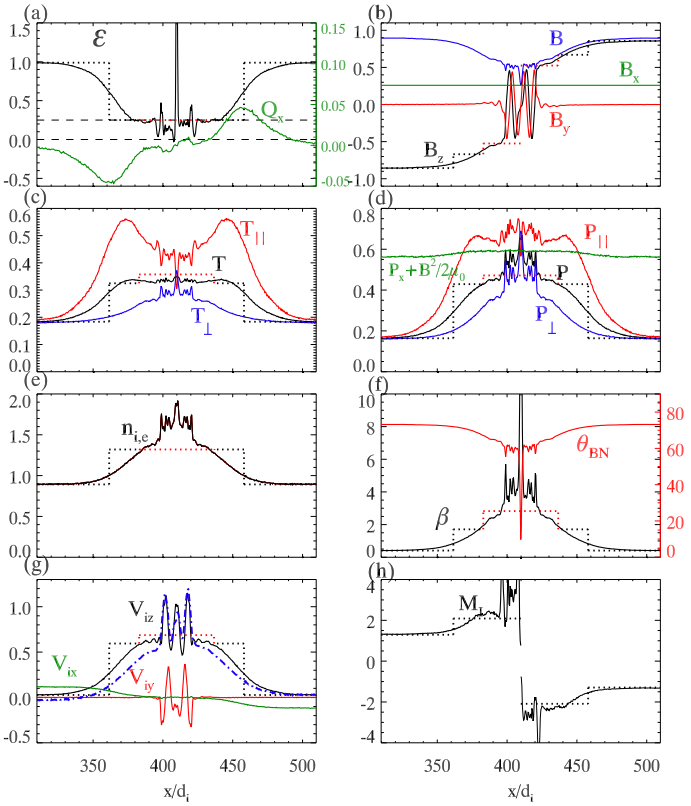

FIG. 3: Profiles of physical quantities of Riemann 75° case with system size $1.6d_i \times 816.2d_i$ at time $200/\Omega_{ci}$ [18] presented in the same format as Fig. 2. The dotted black and red curves are the predicted jumps of an A-SS with $M_{Iu} = 1.29$ followed by the D-SS. Both dotted curves should be compared with the solid black curves.

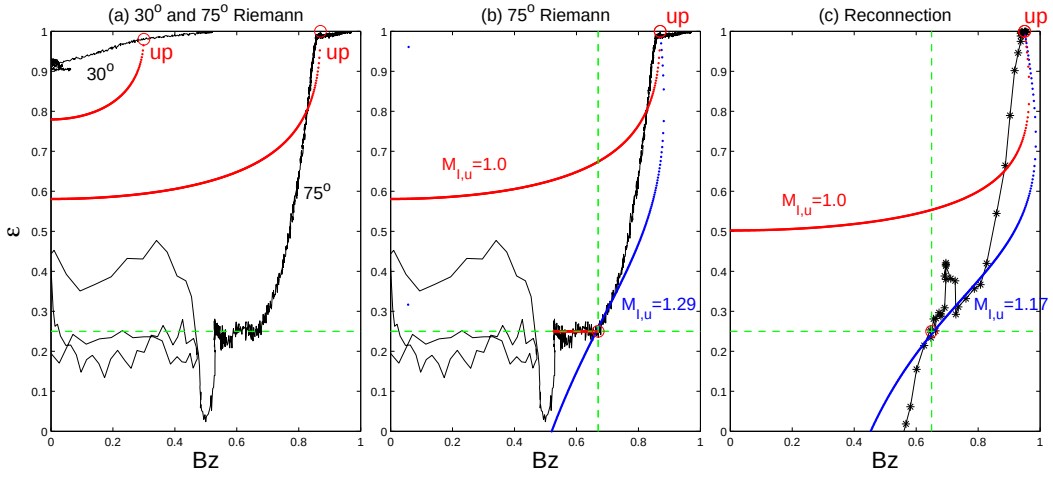

FIG. 4: The $B_z - \varepsilon$ space where the downstream direction is toward $B_z = 0$. In (a) the lower black curve is measured from the right half part of data from the Riemann simulation in Fig. 3 and the upper curve is from a similar simulation with $\theta_{BN} = 30°$. The red curves show possible transitions of a $M_{Iu} = M_{Id} = 1$ slow shock transition (11-SS) from the anisotropic MHD equations. If the red 11-SS curve intersects the black curve at any location other than in the upstream state, the switch-off-slow shock transition is not possible. In (b) the 75° Riemann data in black, the 11-SS transition in red and a $M_{Iu} = 1.29$ SS transition (A-SS) in blue. The intersection of the black and the blue curves at the red circle ($B_z = 0.67, \varepsilon = 0.25$) is the chosen A-SS downstream since this solution allows a transition from ε unity upstream to a downstream value of 0.25. In (c) plots from the reconnection simulation similar to those in (b) for the Riemann 75° case. The red circle ($B_z = 0.65, \varepsilon = 0.25$) is the chosen downstream state.

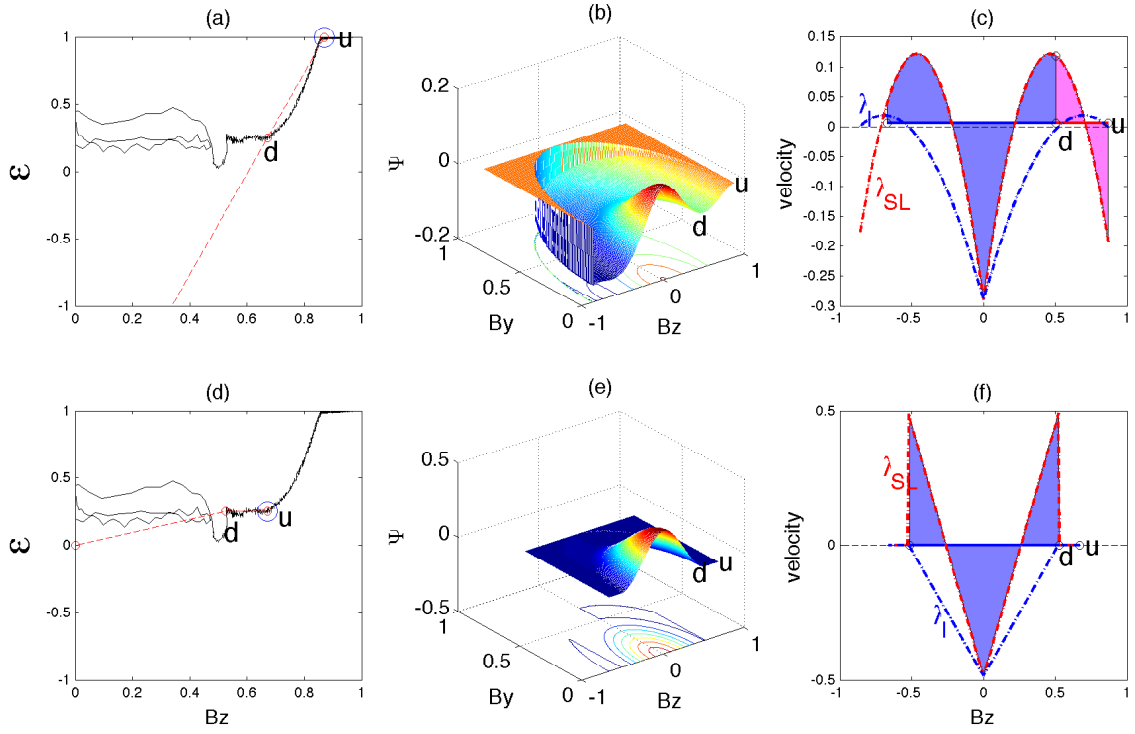

FIG. 5: Analysis of the 75° Riemann simulation. In (a) the $B_z - \varepsilon$ data from the simulation with a chosen analytic relation for $\varepsilon(B_z)$ linking the upstream and downstream states. In (b) the pseudo-potential Ψ from anisotropic derivative nonlinear-Schrödinger-Burgers equations [19] showing the potential minimum at the downstream solution and the barrier preventing the development of the SSS. In (c) the shock speed (red solid) and the slow (dot-dashed red) and intermediate (dot-dashed blue) characteristics, λ_{SL} and λ_I respectively, show that the A-SS solution is a super-intermediate to super-intermediate transition but a super-slow to sub-slow transition. In (d) similar to (a) but with an analytic relation for $\varepsilon(B_z)$ describing the $\varepsilon = 0.25$ plateau region and extension toward $\varepsilon = 0$. In (e) the pseudo-potential for the D-SS showing that the potential is flat between the up and downstream states and the barrier that facilitates a left hand rotation that describes the compound D-SS/RD transition. In (f) wave characteristics for the D-SS/RD as shown in (c).